This is the accepted manuscript made available via CHORUS. The article has been published as:

High-rate subgigahertz-linewidth bichromatic entanglement source for quantum networking

Alexander N. Craddock, Yang Wang, Felipe Giraldo, Rourke Sekelsky, Mael Flament, and Mehdi Namazi

Phys. Rev. Applied **21**, 034012 — Published 8 March 2024

DOI: 10.1103/PhysRevApplied.21.034012

High-rate sub-GHz linewidth bichromatic entanglement source for quantum networking

Alexander N. Craddock, Yang Wang, Felipe Giraldo, Rourke Sekelsky, Mael Flament, and Mehdi Namazi*
Qunnect Inc., 141 Flushing Ave, Ste 1110, Brooklyn, NY 11205-1005
(Dated: January 8, 2024)

The generation of entangled photon pairs which are compatible with quantum devices and standard telecommunication channels are critical for the development of long range fiber quantum networks. Aside from wavelength, bandwidth matching and high fidelity of produced pairs are necessary for high interfacing efficiency. High-rate, robust entanglement sources that satisfy all these conditions remain an outstanding experimental challenge. In this work, we study an entanglement source based on four-wave mixing in a diamond configuration in a warm rubidium vapor. We theoretically and experimentally investigate a new operating regime and demonstrate an entanglement source which produces highly non-degenerate 795 and 1324-nm photon pairs. With this source we are able to achieve in-fiber pair generation rates greater than $10^7\,/s$, orders of magnitude higher than previously reported atomic entanglement sources. Additionally, given our source's native compatibility with telecom infrastructure and atomic systems, it is an important step towards scalable quantum networks.

INTRODUCTION

Entanglement sources are critical in the field of quantum networking, for applications such as distributed quantum computing [1–4], sensing [5–7], and secure communication [8, 9]. For these areas, the sources should be bright, high fidelity, and produce photons which are compatible with both the quantum channels and any quantum devices which are being used. Additionally, these applications will require many of these sources, so it is essential that they be simple and robust.

Spontaneous parametric down-conversion in nonlinear crystals has long been the go-to method for producing entangled pairs of photons [10–13]. However, photons produced in this manner are typically spectrally broad, making them incompatible with devices such as quantum memories, atomic sensors, quantum computers and simulators. While work has been done to narrow the linewidth of these sources using optical cavities [14, 15], this increases the complexity.

Alternatively, there is a growing body of work that utilizes spontaneous four wave mixing (FWM) in both warm and cold atomic vapors to produce narrowband entangled photon pairs [16–20]. While cold atomic systems have proven a good platform for studying this phenomenon, they require complex experimental setups which make their widespread use outside the lab prohibitive. Conversely, warm-atomic ensembles are a natural system for implementing entanglement sources given their compactness, robustness, simplicity, and native compatibility with atom-based quantum devices.

Early work on FWM in warm ensembles leveraged a diamond level system in rubidium atoms to generate bichromatic polarization entangled photon pairs at telecom and near-infrared (NIR) wavelengths [18], useful for interfacing atomic quantum devices through fiber networks. However, these entanglement sources were limited to low absolute brightness (pairs per unit time), $\approx 5\times10^3\,/s$, attributed to the inability to simultaneously address all the velocity groups within the vapor in the photon production process [21]. Recent literature on the topic has focused on FWM in a ladder scheme with near-degenerate wavelengths [16, 17, 22, 23]. There, higher absolute brightness entanglement sources, $\approx 2\times10^4\,/s$, have been demonstrated, but the output photons are necessarily close in wavelength restricting their utility. In addition to entanglement sources, there exists work on pair sources based on warm atomic ensembles. For these sources high absolute brightness, $\approx 8\times10^5\,/s$, and high spectral brightnesses (pairs per unit time per unit bandwidth), $\approx 4\times10^5/s/$MHz, have been demonstrated in ladder [24] and double Λ configurations [25] respectively.

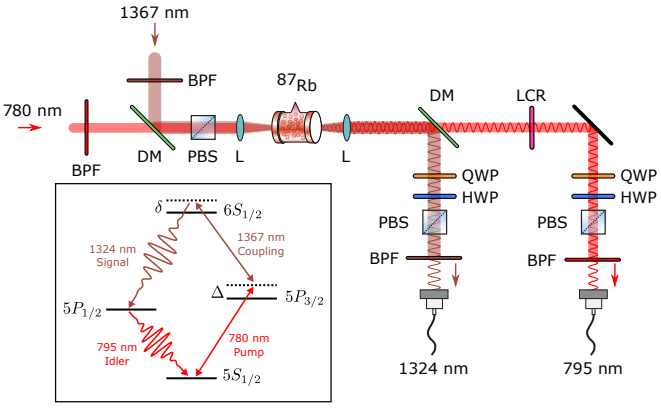


FIG. 1. Experimental setup for generation and analysis of entangled photon pairs. Inset: Relevant rubidium level diagram for the four-wave mixing process. PBS: polarizing beam splitter, DM: dichroic mirror, BPF: bandpass filter, LCR: liquid crystal retarder, QWP: quarter waveplate, HWP: half waveplate, L: Lens.

In this paper, we demonstrate a source of bichromatic entangled photon pairs based on diamond-scheme FWM

in a warm rubidium ensemble with high absolute and spectral brightness. We theoretically and experimentally explore a new operating regime in the diamond scheme that allows us to address all the atoms within the vapor, which we believe to be a general result not unique to our system. We achieve entangled pair rates in-fiber exceeding $\approx 10^7/s$, with a lower bound on the $|\Phi_+\rangle$ Bell state fidelity of $> 95\%$. To the best of our knowledge this is the highest demonstrated absolute brightness for a warm-atom entangled photon pair source. Additionally, the source produces narrowband telecom-NIR entangled photon pairs (1324 and 795 nm respectively), making our source well suited for interfacing quantum devices over optical fibers.

EXPERIMENTAL SETUP

In this work we explore spontaneous FWM in a warm ^{87}Rb vapor. The relevant atomic level structure for the diamond FWM process is shown inset in Fig. 1. We use a 780-nm pump and 1367-nm coupling laser to drive the two-photon $|5S_{1/2}\rangle \rightarrow |6S_{1/2}\rangle$ transition, via the intermediate $|5P_{3/2}\rangle$ state. The pump light is frequency stabilized to the ^{85}Rb $|5S_{1/2}, F=3\rangle \rightarrow |5P_{3/2}, F'=4\rangle$ transition, and thus $\Delta/2\pi \approx 1.1$ GHz (blue detuned from the ^{87}Rb $|5S_{1/2}, F=2\rangle \rightarrow |5P_{3/2}, F'=3\rangle$ transition). To stabilize the coupling light we use a dual resonance optical pumping (DROP) setup [26]. We use an electro-optic modulator (EOM) to allow us to offset the detuning of the 1367-nm light from resonance.

The experimental setup is shown in Fig. 1. The pump and coupling beams are overlapped on a dichroic mirror so that they co-propagate through a 5-mm long enriched ^{87}Rb vapor cell. Both the pump and coupling beams are horizontally polarized prior to the vapor cell using a common polarizing beamsplitter (PBS). We use a pair of $f \approx 50$ mm achromatic lenses to focus the beams to a $1/e^2$ beam radii of ≈ 30 μm inside the cell. We collect the 1324-nm signal, and 795-nm idler at zero angle to the pump, which naturally satisfies the phase matching condition [27]. Both signal and idler are coupled into collimators with equivalent $1/e^2$ mode radii of ≈ 20 μm in the vapor cell. We heat the cell using a pair of metal ceramic heaters placed directly on the faces of the cell.

After the cell we use a dichroic mirror to separate the telecom and NIR light. We use bandpass filters to suppress leakage of the coupling and pump beams into the signal and idler fibers. On the signal and idler paths, a quarter waveplate (QWP), half waveplate (HWP), and PBS allow us to select the detected polarization modes. We align a liquid crystal retarder (LCR) on the idler path so that the slow axis is in the vertical direction. By tuning the retardance we can apply arbitrary phase shifts between the $|H\rangle$ and $|V\rangle$ polarization modes.

We detect the idler photons using a single photon avalanche photodiode, and the signal photons using a superconducting nanowire single photon detector (≈ 350-ps and ≈ 90-ps timing jitter respectively). The detection efficiency, which includes only the quantum efficiencies of the detectors and post fiber coupling losses, is 78(2)% and 68% for the signal and idler photons respectively.

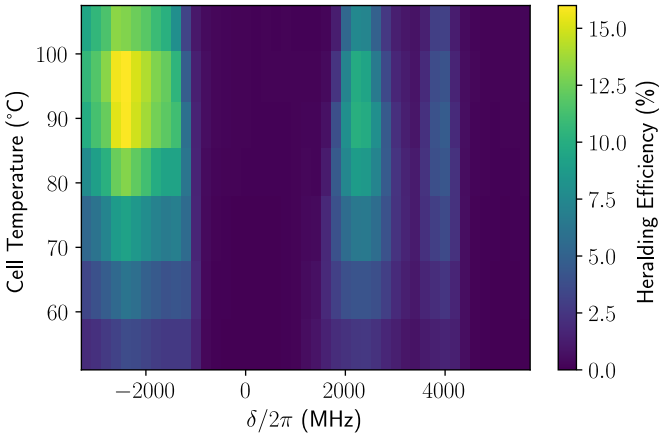


FIG. 2. Heralding efficiency of the source as a function of the spectroscopically measured vapor cell temperature, and the two-photon detuning, δ. The single photon detuning is fixed, $\Delta/2\pi \approx 1.1$ GHz. The pump power is fixed at ≈ 250 μW. For each detuning/temperature we vary the coupling power to set the signal rate to ≈ 100 kcps.

RESULTS

We first explore the dependence of the source parameters on the two-photon detuning and the vapor cell optical depth (OD, measured for 795-nm idler photons). To adjust the OD we change the vapor temperature, while the two-photon detuning is varied using the EOM in the offset DROP lock. For this data we fix the pump power at ≈ 250 μW, and vary the coupling power to bring the detected signal rate to ≈ 100 kcps. Here, we only measure the $|VV\rangle$ mode of the source.

We look at the heralding efficiency, the probability of detecting a 795-nm photon upon the detection of a 1324-nm photon. In Fig. 2, for fixed atomic temperature, we see that increasing two-photon detuning increases the heralding efficiency.

To understand this behavior we analyze the three level Hamiltonian associated with the excitation process, under the rotating wave approximation, for an atom with velocity, v

$$\hat{H}(v) = \hbar \begin{pmatrix} 0 & \frac{\Omega_p}{2} & 0 \\ \frac{\Omega_p^*}{2} & -\Delta(v) & \frac{\Omega_c}{2} \\ 0 & \frac{\Omega_c^*}{2} & -\delta(v) \end{pmatrix}, \tag{1}$$

in the $\{|5S_{1/2}\rangle, |5P_{3/2}\rangle, |6S_{1/2}\rangle\}$ basis. We treat the $|6S_{1/2}\rangle \rightarrow |5P_{1/2}\rangle \rightarrow |5S_{1/2}\rangle$ as an effective $|6S_{1/2}\rangle \rightarrow$

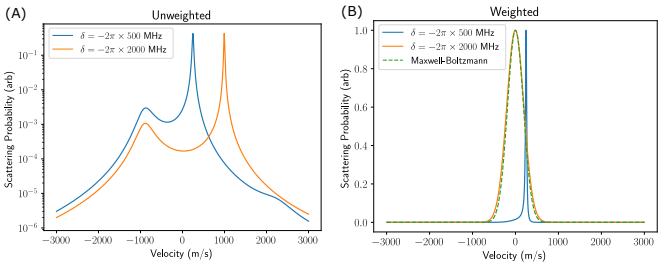


FIG. 3. Numerical simulations of the simplified three-level system in the near (blue) and far-off (orange) two-photon resonance regimes. Plot (A) ((B)) shows the scattering probability, unweighted (weighted) by the Maxwell-Boltzmann distribution, as a function of atomic velocity. (B) has been renormalized so that the peak weighted scattering probability is unity for ease of comparison. Dashed green line in (B) shows the Maxwell Boltzmann distribution for vapor temperature used in the simulation. In both cases the pump detuning is fixed far from resonance ($\Delta/2\pi = 1150$ MHz), the pump and coupling Rabi frequencies are held at reasonable experimental values ($\Omega_p/2\pi = \Omega_c/2\pi = 350$ MHz), and temperature is fixed at $T = 80°$ C.

$|5S_{1/2}\rangle$ decay, in addition to the $|6S_{1/2}\rangle \rightarrow |5P_{3/2}\rangle$ and $|5P_{3/2}\rangle \rightarrow |5S_{1/2}\rangle$ decay channels.

We treat atomic motion as one dimensional along the beam propagation direction. This is a valid approximation for our collinear experimental geometry. The large single photon detuning used in the experiment avoids significantly populating the $|5P_{3/2}\rangle$ state. We numerically solve for the steady state of the Liouvillian associated with the reduced three-level system. As the $|6S_{1/2}\rangle \rightarrow |5P_{1/2}\rangle$ decay rate is proportional to the $|6S_{1/2}\rangle$ steady state population, we use this as a proxy for the signal photon scattering probability. In Fig. 3(A) we show two examples of the scattering probability as a function of atomic velocity to demonstrate the near (blue) and far-off (orange) two-photon resonant regimes. In both regimes a sharp resonant peak ($v \approx 250$m/s and $v \approx 1000$m/s for the near and far detuned case in Fig. 3(A)) is seen in the scattering probability at

$$v \approx -\frac{c\delta}{\omega_{6S_{1/2}}}, \tag{2}$$

due to the two-photon Doppler shift, where $\hbar\omega_{6S_{1/2}}$ is the energy of the $|6S_{1/2}\rangle$ state. Two broader and less prominent peaks are seen in the figure at $v \approx -1000$m/s, where the $|5P_{3/2}\rangle$ state is resonantly excited. To determine the scattering probability in the atomic vapor we weight the $|6S_{1/2}\rangle$ population by the Maxwell-Boltzmann distribution, shown in Fig. 3(B). For the near detuned case a significant fraction of the population resides at the resonant velocity class, giving rise to a sharp feature in the figure. However, for the far-off two-photon resonance regime the resonant velocity has a near negligible population fraction. After weighting we find that the majority of the scattering occurs off-resonantly despite the unweighted scattering probability for this process being significantly smaller than for resonant scattering. As seen in Fig. 3(B), for far-off two-photon resonance excitation the weighted scattering probability follows the Maxwell-Boltzmann distribution.

The significance of this behavior can be understood by considering the collective excitation projected onto the atomic system upon detection of a signal photon [28]. The likelihood of phase matched emission of the idler scales with the atom number participating in the collective excitation [29]. Given that the collective excitation has a distribution similar to that of the weighted scattering probability, we expect, for a fixed atomic density, phase matched emission of the idler to be more likely for off-resonant excitation relative to near-resonant excitation. For a given vapor temperature, we therefore expect higher heralding efficiencies when the source is operated in the far-off-resonant regime as seen in Fig. 2.

While the technique has been presented for the specific diamond scheme shown inset in Fig. 1, we believe it is generally applicable, and is potentially responsible for the behavior observed in a different diamond scheme in [30].

From our theory model we expect the source behavior to be symmetric about zero two-photon detuning. However, we see that is not the case in Fig. 2. We attribute this to undesired interaction with ^{85}Rb atoms within the vapor at positive two-photon detunings ($\approx$ 99% ^{87}Rb vapor cell purity). Additionally, we would expect the heralding efficiency to saturate to a constant value at large two-photon detunings. However, we see a clear peak in the heralding efficiency as the two-photon detuning is increased. We believe this is related to the increased coupling power needed at large two-photon detunings.

In addition to a trend as the two-photon detuning is changed, for fixed two-photon detuning, we see a peak in the heralding efficiency as the vapor cell temperature is altered. This phenomenon has been previously observed [28] and is attributed to the competing processes of an increase in directed collective emission, and decrease in idler photon transmission, as the vapor temperature, and therefore OD, is increased.

For the remainder of this paper we operate with a two-photon detuning of $\delta/2\pi \approx -2400$ MHz and a cell temperature $\approx 93°$ C (measured spectroscopically), where the maximum measured heralding efficiency is, ≈ 16 % (≈ 24 % corrected for idler detection efficiency). This is comparable to the detector corrected heralding efficiency observed with nearly-Doppler-free ladder pair sources [24]. Here, the resonant OD of the cell for the idler photons is ≈ 9.

Next, we investigate scaling properties of the source with the coupling and pump powers. We again only measure the $|VV\rangle$ mode of the source. In Fig. 4(A) we show how the coincidence rate varies with the pump and coupling powers. For low pump and coupling power

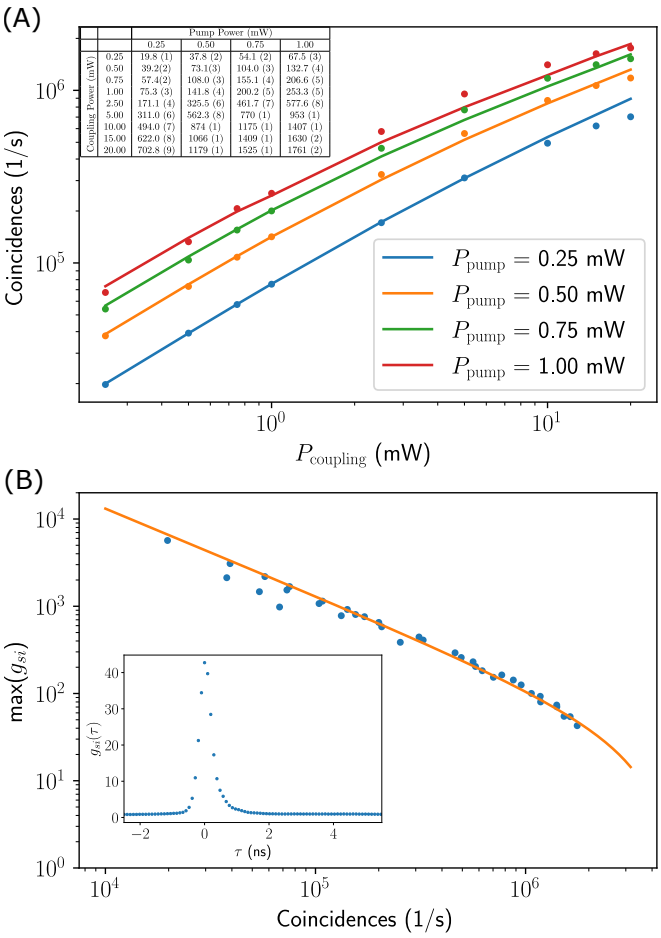


FIG. 4. Scaling behavior of the source with pump and coupling power. (A) displays measured signal-idler coincidence rate as a function of coupling power, for various pump powers. We use a $\propto P_{coupling}P_{pump}$ fit that accounts for the finite detector dead times. We calculate a measured scaling constant of the $|VV\rangle$ mode coincidence rate $\approx 3\times10^5\,/s/\text{mW}^2$ ($\approx 6\times10^5\,/s/\text{mW}^2$ when accounting for detection efficiencies). Inset table displays the coincidence values displayed in the plot. (B) shows the peak value of the signal-idler cross-correlation, g_{si}, as a function of the $|VV\rangle$ mode coincidence rate. Orange line is a $\propto$ 1/Coincidences fit, taking into account the finite detector dead time in the system. Inset displays a typical g_{si} curve, using 100-ps bins. In both plots error bars, arising from statistical uncertainties, are smaller than the data points.

we see a near-linear scaling in the coincidence rate as function of power, with a measured scaling constant of $\approx 3\times10^5\,/s/\text{mW}^2$ ($\approx 6\times10^5\,/s/\text{mW}^2$ when accounting for detection efficiencies). At high power we observe a saturation in the coincidence rate for increasing power. This is partly due to the finite dead time of the detectors ($\approx$ 20 ns for both signal and idler), which we account for in the fit shown in the figure. However, we have repeated the measurements, using neutral density filters on both the signal and idler paths to reduce this issue, and still observe deviation from linearity at higher coupling powers. We attribute this to saturation of the atomic medium.

Similar to other sources, as the pair production rate is increased, we expect the signal-idler cross-correlation function, g_{si} to decrease. We show the scaling of the maximum value of g_{si} with coincidences in Fig. 4(B), with a typical curve of g_{si} as a function of the delay time between detections, τ, shown inset. In theory $g_{si} \propto 1/\text{Coincidences}$. We observe this inverse scaling for low coincidence rates. However, for high coincidence rates we see a deviation from this behavior. We attribute this to the finite detector dead time, as this is not seen when the measurement is repeated using neutral density filters on the signal and idler arms. We take this detector saturation into account in the model in the figure.

At the maximum used powers of 1 and 20 mW, for the pump and coupling beams respectively (used for the remainder of the paper), the measured $|VV\rangle$ mode coincidence rate is $\approx 1.7\times10^6/s$ with $g_{si}\approx 40$, corresponding to a $|VV\rangle$ mode rate of $\approx 5\times10^6/s$, when correcting for detection efficiency and dead time saturation of the detectors.

From the g_{si} curve, shown inset in Fig. 4(B), we estimate the biphoton linewidth to be under $2\pi\times 1$ GHz (after deconvolving the finite response time of the detectors), similar to that in the ladder-type FWM systems where all velocity classes participate in the collective excitation [28]. This value is corroborated by stimulated FWM biphoton measurements, similar to those in [31]. We attribute the biphoton bandwidth to the convolution of the Doppler broadened emission and the absorption of the idler as it propagates through the cell. While not explored here, we do expect similar variability of the bandwidth with OD as in [28]. We note that this bandwidth is comparable to those demonstrated by existing warm atom quantum memories [32, 33], opening the door for an all warm-atom based telecom compatible quantum repeater.

With the pumping scheme used, and the rubidium Zeeman structure, we expect the source to produce $|\Phi_+\rangle = \frac{1}{\sqrt{2}}(|HH\rangle + |VV\rangle)$ entangled pairs [18]. We find that the dichroic used to separate the signal and idler photons, and mirrors used to couple the signal and idler photons into their respective fibers, adds an arbitrary but stable phase shift between the $|HH\rangle$ and $|VV\rangle$ modes. We tune the retardance of the LCR to compensate these phase shifts, and recover the $|\Phi_+\rangle$ state. To verify the entangled state produced after this operation, we perform two-photon tomography. We use neutral density filters with $OD \approx 1$ on both the signal and idler paths to ensure there are no issues with detector saturation during the tomography. Using the maximum likelihood method discussed in [34] we reconstruct the density matrix for the two-photon state, shown in Fig. 5. From the reconstructed density matrix we place a lower bound fidelity to the $|\Phi_+\rangle$ Bell state of 95%[35], for an entangled pair

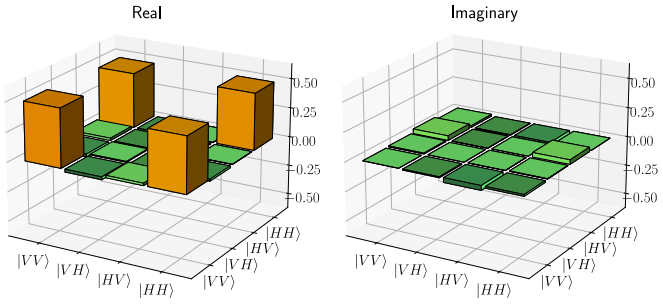


FIG. 5. Real and imaginary parts of the maximum-likelihood density matrix reconstruction of the signal-idler state. Lower bound on the fidelity to the expected $|\Phi_+\rangle$ Bell state is 95%.

rate greater than $10^7\,/s$.

CONCLUSION

The development of large-scale quantum networks relies on the deployment of practical entanglement sources that operate with high pair generation rate, narrow linewidth, high fidelity and wavelength compatibility with telecom and quantum devices. We have theoretically and experimentally investigated a new operating regime for warm-atom FWM entangled photon sources in the diamond configuration that can satisfy all the above conditions simultaneously. Under these conditions, we are able to address all the velocity groups within a vapor, enabling us to achieve an entangled in-fiber pair absolute brightness greater than $10^7/s$. Given the sub GHz bandwidth of the biphotons produced, the corresponding spectral brightness is $\approx 10^4/s/\text{MHz}$. To the best of our knowledge, this is the highest absolute and spectral brightness achieved for a warm-atom entangled photon source. We have demonstrated that the bichromatic photon pairs (1324 and 795 nm) are well correlated, $g_{si} \geq 40$, and from maximum likelihood estimation we place a lower bound on the fidelity to the $|\Phi_+\rangle$ Bell state of 95%. Given that our source produces entangled pairs that are compatible both with telecom infrastructure and existing quantum devices, it has applications for quantum repeating, distributed quantum processing, and quantum enhanced sensor networks. Additionally, the relative simplicity of the source allows for the development of robust devices for integrating into existing telecom infrastructure.

ACKNOWLEDGMENTS

We thank the Qunnect Inc. team, especially Noel Goddard, for their help with manuscript preparation. This work is supported by the U.S. Department of Energy under award no. DE-SC0021556.

* Corresponding author. mehdi@quconn.com

[1] C. Monroe, R. Raussendorf, A. Ruthven, K. R. Brown, P. Maunz, L.-M. Duan, and J. Kim, Large-scale modular quantum-computer architecture with atomic memory and photonic interconnects, Phys. Rev. A **89** (2014).
[2] S. Pirandola and S. L. Braunstein, Physics: Unite to build a quantum internet, Nature **532**, 169 (2016).
[3] S. Wehner, D. Elkouss, and R. Hanson, Quantum internet: A vision for the road ahead, Science **362**, eaam9288 (2018).
[4] H. J. Kimble, The quantum internet, Nature **453**, 1023 (2008).
[5] Z. Eldredge, M. Foss-Feig, J. A. Gross, S. L. Rolston, and A. V. Gorshkov, Optimal and secure measurement protocols for quantum sensor networks, Phys. Rev. A **97** (2018).
[6] E. T. Khabiboulline, J. Borregaard, K. De Greve, and M. D. Lukin, Optical interferometry with quantum networks, Phys. Rev. Lett. **123**, 070504 (2019).
[7] T. J. Proctor, P. A. Knott, and J. A. Dunningham, Multiparameter estimation in networked quantum sensors, Phys. Rev. Lett. **120**, 080501 (2018).
[8] A. K. Ekert, Quantum cryptography based on bell's theorem, Phys. Rev. Lett. **67**, 661 (1991).
[9] C. H. Bennett, G. Brassard, and N. D. Mermin, Quantum cryptography without bell's theorem, Phys. Rev. Lett. **68**, 557 (1992).
[10] P. G. Kwiat, K. Mattle, H. Weinfurter, A. Zeilinger, A. V. Sergienko, and Y. Shih, New high-intensity source of polarization-entangled photon pairs, Phys. Rev. Lett. **75**, 4337 (1995).
[11] J. Yin, Y. Cao, Y.-H. Li, S.-K. Liao, L. Zhang, J.-G. Ren, W.-Q. Cai, W.-Y. Liu, B. Li, H. Dai, G.-B. Li, Q.-M. Lu, Y.-H. Gong, Y. Xu, S.-L. Li, F.-Z. Li, Y.-Y. Yin, Z.-Q. Jiang, M. Li, J.-J. Jia, G. Ren, D. He, Y.-L. Zhou, X.-X. Zhang, N. Wang, X. Chang, Z.-C. Zhu, N.-L. Liu, Y.-A. Chen, C.-Y. Lu, R. Shu, C.-Z. Peng, J.-Y. Wang, and J.-W. Pan, Satellite-based entanglement distribution over 1200 kilometers, Science **356**, 1140 (2017).
[12] J. Yin, J.-G. Ren, H. Lu, Y. Cao, H.-L. Yong, Y.-P. Wu, C. Liu, S.-K. Liao, F. Zhou, Y. Jiang, X.-D. Cai, P. Xu, G.-S. Pan, J.-J. Jia, Y.-M. Huang, H. Yin, J.-Y. Wang, Y.-A. Chen, C.-Z. Peng, and J.-W. Pan, Quantum teleportation and entanglement distribution over 100-kilometre free-space channels, Nature **488**, 185 (2012).
[13] M. Giustina, M. A. M. Versteegh, S. Wengerowsky, J. Handsteiner, A. Hochrainer, K. Phelan, F. Steinlechner, J. Kofler, J.-Å. Larsson, C. Abellán, W. Amaya, V. Pruneri, M. W. Mitchell, J. Beyer, T. Gerrits, A. E. Lita, L. K. Shalm, S. W. Nam, T. Scheidl, R. Ursin, B. Wittmann, and A. Zeilinger, Significant-loophole-free test of bell's theorem with entangled photons, Phys. Rev. Lett. **115**, 250401 (2015).
[14] H. Wang, T. Horikiri, and T. Kobayashi, Polarization-entangled mode-locked photons from cavity-enhanced spontaneous parametric down-conversion, Phys. Rev. A **70** (2004).
[15] X.-H. Bao, Y. Qian, J. Yang, H. Zhang, Z.-B. Chen, T. Yang, and J.-W. Pan, Generation of narrow-band polarization-entangled photon pairs for atomic quantum memories, Phys. Rev. Lett. **101**, 190501 (2008).

[16] J. Park, H. Kim, and H. S. Moon, Polarization-entangled photons from a warm atomic ensemble using a sagnac interferometer, Phys. Rev. Lett. **122**, 143601 (2019).

[17] J. Park, J. Bae, H. Kim, and H. S. Moon, Direct generation of polarization-entangled photons from warm atomic ensemble, Appl. Phys. Lett. **119**, 074001 (2021).

[18] R. T. Willis, F. E. Becerra, L. A. Orozco, and S. L. Rolston, Photon statistics and polarization correlations at telecommunications wavelengths from a warm atomic ensemble, Opt. Express **19**, 14632 (2011).

[19] T. Chanelière, D. N. Matsukevich, S. D. Jenkins, T. A. B. Kennedy, M. S. Chapman, and A. Kuzmich, Quantum telecommunication based on atomic cascade transitions, Phys. Rev. Lett. **96**, 093604 (2006).

[20] G. K. Gulati, B. Srivathsan, B. Chng, A. Cerè, and C. Kurtsiefer, Polarization entanglement and quantum beats of photon pairs from four-wave mixing in a cold87rb ensemble, New J. Phys. **17**, 093034 (2015).

[21] Y.-S. Lee, S. M. Lee, H. Kim, and H. S. Moon, Highly bright photon-pair generation in doppler-broadened ladder-type atomic system, Opt. Express **24**, 28083 (2016).

[22] J. Park, H. Kim, and H. Seb Moon, Entanglement swapping with autonomous polarization-entangled photon pairs from a warm atomic ensemble, Opt. Lett. **45**, 2403 (2020).

[23] J. Park, H. Kim, and H. S. Moon, Four-photon greenberger-horne-zeilinger entanglement via collective two-photon coherence in doppler-broadened atoms, Adv. Quantum Technol. **4**, 2000152 (2021).

[24] O. Davidson, O. Yogev, E. Poem, and O. Firstenberg, Bright, low-noise source of single photons at 780 nm with improved phase-matching in rubidium vapor, arXiv:2301.06049.

[25] J.-M. Chen, C.-Y. Hsu, W.-K. Huang, S.-S. Hsiao, F.-C. Huang, Y.-H. Chen, C.-S. Chuu, Y.-C. Chen, Y.-F. Chen, and I. A. Yu, Room-temperature biphoton source with a spectral brightness near the ultimate limit, Phys. Rev. Res. **4** (2022).

[26] A. Pérez Galván, Y. Zhao, and L. A. Orozco, Measurement of the hyperfine splitting of the $6S_{1/2}$ level in rubidium, Phys. Rev. A **78** (2008).

[27] R. T. Willis, F. E. Becerra, L. A. Orozco, and S. L. Rolston, Correlated photon pairs generated from a warm atomic ensemble, Phys. Rev. A **82** (2010).

[28] O. Davidson, R. Finkelstein, E. Poem, and O. Firstenberg, Bright multiplexed source of indistinguishable single photons with tunable GHz-bandwidth at room temperature, New J. Phys. **23**, 073050 (2021).

[29] M. Saffman and T. G. Walker, Creating single-atom and single-photon sources from entangled atomic ensembles, Phys. Rev. A **66** (2002).

[30] D.-S. Ding, W. Zhang, S. Shi, Z.-Y. Zhou, Y. Li, B.-S. Shi, and G.-C. Guo, Hybrid-cascaded generation of tripartite telecom photons using an atomic ensemble and a nonlinear waveguide, Optica **2**, 642 (2015).

[31] T. Jeong, J. Park, and H. S. Moon, Stimulated measurement of spontaneous four-wave mixing from a warm atomic ensemble, Phys. Rev. A (Coll. Park.) **100** (2019).

[32] R. Finkelstein, E. Poem, O. Michel, O. Lahad, and O. Firstenberg, Fast, noise-free memory for photon synchronization at room temperature, Sci. Adv. **4**, eaap8598 (2018).

[33] G. Buser, R. Mottola, B. Cotting, J. Wolters, and P. Treutlein, Single-photon storage in a ground-state vapor cell quantum memory, PRX quantum **3** (2022).

[34] D. F. V. James, P. G. Kwiat, W. J. Munro, and A. G. White, Measurement of qubits, Phys. Rev. A **64** (2001).

[35] Lower bound is the minimum value attained when varying the minimization solver and initial conditions.